A Modular Bidirectional Topology for Grid-Tied PV Powered EV Chargers with Isolated Single-Stage Sub-Modules

Fatemeh Nasr Esfahani
Smith Engineering,
Queen's University
Kingston, ON, Canada
f.nasresfahani@lancaster.ac.uk

Javad Ebrahimi
Smith Engineering,
Queen's University
Kingston, ON, Canada
javad.ebrahimi@queensu.ca

Alireza Bakhshai
Smith Engineering,
Queen's University
Kingston, ON, Canada
alireza.bakhshai@queensu.ca

Xiandong Ma
School of Engineering,
Lancaster University
Lancaster, UK
xiandong.ma@lancaster.ac.uk

Ahmed Darwish
School of Engineering,
Lancaster University
Lancaster, UK
a.badawy@lancaster.ac.uk

Abstract— **Renewable energy sources (RES) such as solar photovoltaic (PV) are employed in electric vehicle (EV) charging stations to promote sustainable transportation and reduce the load on the AC grid. This paper introduces a modular power converter topology that interfaces with solar PV, EV batteries, and the AC grid. The proposed topology supports EV battery charging in two modes: DC/DC (from PV modules) and AC/DC (from the AC grid). Additionally, during peak hours, EV batteries can function as energy storage units (ESUs) in vehicle-to-grid (V2G) mode. A central element of the proposed topology is the submodule (SM), which is implemented as a single-stage isolated bidirectional Cuk-based converter. This converter is chosen for its exceptional features, including high efficiency and inherent power factor correction (PFC) due to continuous input and output currents. The paper first details the operating modes of the Cuk-based SM. To improve performance, an extra switching state is added in the AC/DC (rectifier) mode, enabling the second-order harmonic from the AC grid to be stored within the Cuk SM instead of being passed to the battery. Additionally, power losses at the SM level are examined, and the effectiveness of the proposed topology is demonstrated through experimental results.**

Keywords— Photovoltaic (PV), Electric vehicles (EVs), Cuk converter, Grid-tied topology, Vehicle-to-grid (V2G)

I. INTRODUCTION

The environmental benefits of electric vehicles (EVs) are maximized when they are charged using eco-friendly energy sources such as solar photovoltaic (PV) [1]-[2]. Since PV modules generate DC power, they can be used to directly charge EVs, which not only lowers operational costs but also decreases reliance on the AC grid [3]. Furthermore, EV batteries can function as energy storage units (ESUs), storing surplus power from the AC grid and feeding it back into the grid during peak hours through vehicle-to-grid (V2G) mode [4]-[8].

Power converter topologies used in PV-grid charging stations typically include a DC/DC converter with built-in maximum power point tracking (MPPT), a DC/DC converter on the EV side, and a voltage-source inverter (VSI) on the grid side [4]. A classic method of classifying these power converter topologies is to distinguish between non-integrated and integrated systems. There are at least three converters in non-integrated architectures: (i) a bidirectional grid-interfacing DC/AC converter [9]-[11] (ii) a unidirectional PV-interfacing DC/DC converter [12]-[13], and (iii) a bidirectional EV-interfacing DC/DC converter [14]-[16]. A proper controller for each converter is required to ensure that it charges efficiently, which results in complexity and power losses. In contrast, integrated topologies include sub-converters that interconnect PV, EV batteries, and the grid within a single system [4].

A three-port 10 kW EV charger was introduced in [17], featuring a bidirectional VSI, a unidirectional DC/DC interleaved boost converter, and a bidirectional isolated DC/DC interleaved Flyback converter to interface with the AC grid, PV modules, and EV batteries. There are several benefits associated with this integrated topology, including electrical isolation, high power density, and bidirectional power flow (for support of V2G). By combining silicon carbide (SiC) power devices with an interleaved structure and a high switching frequency, this power solution is capable of significantly higher peak and partial load efficiency than previous solutions. An alternative to this approach is an isolated four-port converter designed to interface with EVs, grids, PVs, and energy storage units [18]. The system consists of a DC/DC unidirectional boost converter for the PV port, a bidirectional converter for the grid port, a triple active bridge (TAB) converter, and a bidirectional DC/DC converter for the EV battery. There are, however, some challenges with these multi-port architectures, such as hard switching in high-power applications and complex control and modulation techniques for the sub-converters. In [19], a three-port integrated topology featuring dual active bridge (DAB) converters on the grid side and an interleaved boost converter on the EV and PV sides were presented. As a result, this design avoids complex controls or optimizations and features a compact and simple layout. However, to achieve lower total harmonic distortion (THD), a substantial output filter is required. A three-port integrated topology was developed in [20] to interface with the grid, PV, and EV. Several sub-converters are used, including DC/DC bidirectional half-bridge converters for the PV and EV ports and an AC/DC bidirectional full-bridge converter to interface the utility grid. Despite offering high power density, unity power factor, low THD, and V2G power flow, this topology is limited by the lack of electrical isolation and hard switching, which are important considerations for EV charging systems [7].

In this paper, a new modular topology is proposed to interface with PV modules, EV batteries, and the AC grid. The design incorporates a single-stage Cuk-based converter as the submodule (SM). The Cuk-based SMs can operate in three modes: DC/DC (from PV to batteries), DC/AC (from PV or batteries to the AC grid), and AC/DC (from the AC grid to the batteries). Besides providing electrical isolation and bidirectional power flow (V2G support), the proposed topology offers low THD and reduced voltage/current stress. The operating modes of the Cuk-based SM are described in detail, and the required duty-cycle ratios for each mode are derived. Additionally, to avoid the oscillating power containing the 2nd order harmonic being transferred to the battery side, an extra switching state is added to the AC/DC (rectifier) operating mode.

The rest of the paper is organized as follows: the proposed topology and its operation modes are presented in Sections II and III, respectively. Second-order harmonic elimination is provided in Section IV. Power losses at the SM level are discussed in Section V. Experimental results are presented in Section VI. Finally, the paper is concluded in Section VII.

II. The Modular Power Converter Topology

Fig. 1 shows the three-phase layout of the proposed topology. The isolated bidirectional single-stage Cuk-based converters are used as submodules (SM) to interface with the PV modules, the battery packs, and the AC grid. Relay switches can be used in experiments to shift between different operating modes. The Cuk-based SM consists of five semiconductor switches (S_P, $S_1 \rightarrow S_4$), two inductors L_1 and L_2, three capacitors C_1, C_2, and C_o, and a high-frequency (HF) transformer with the turn ratio N_S:N_P.

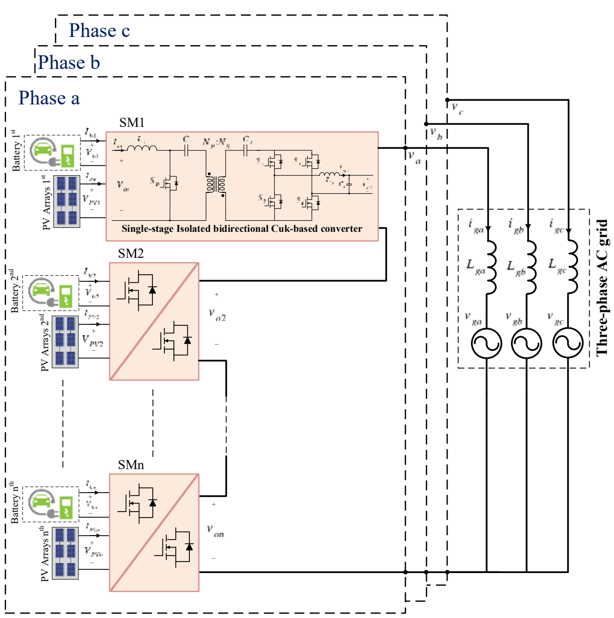

Fig. 1. The three-phase layout of the modular grid-tied PV-powered EV charger topology

III. Operating Modes

A. Mode 1: DC/DC (from PV to EV batteries)

Fig. 2 shows the Cuk-based SM converter when the power flows from the PV modules to the EV batteries. The equivalent circuit of the proposed Cuk-based SM in the DC/DC modes during different subintervals and the related waveforms are presented in Fig. 2(a)-(c), where t_s and t_{ON} are defined as the switching time and ON time, respectively.

Subinterval 1 [$0 \leq t < t_{ON}$]: During this subinterval (see Fig. 2(a)), the switch S_P is turned ON, so the input inductor L_1 is charged by the input voltage source, and its current i_{in} is increasing. The switches, S_1 and S_2 are also in the ON-state, so the capacitors C_1 and C_2 are discharging into the output inductor L_2, increasing the output current i_o.

Subinterval 2 [$t_{ON} \leq t < t_s$]: During this subinterval (see Fig. 2(b)), the switch S_P is in the OFF-state, so the input inductor L_1 is discharging into the capacitors C_1 and C_2. The switch S_2 is turned ON, discharging the output inductor L_o and decreasing its current i_o.

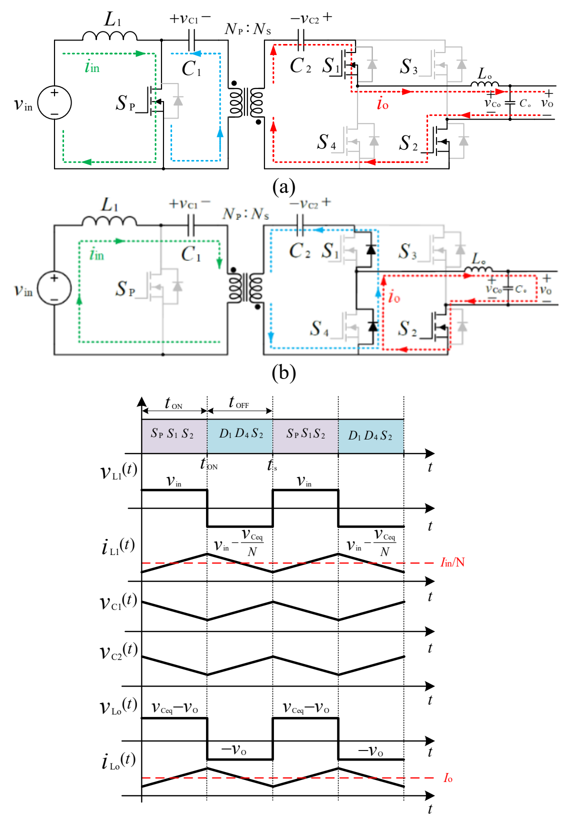

Fig. 2. Switching principles during DC/DC mode (a) $0<t<t_{ON}$ (b) $t_{ON}<t<t_s$ (c) key waveforms

B. Mode 2: AC/DC (AC grid to EV batteries)

Thanks to the bidirectional feature of the proposed topology, current can flow from the AC grid to the HV battery packs. During charging mode, each SM operates as an AC/DC rectifier. The equivalent circuit of the proposed Cuk-based SM during different subintervals and the related waveforms are presented in Fig. 3.

Subinterval 1 [$0 \leq t < d_1 t_s$]: Fig. 3(a) shows the Cuk-based SM converter during charging mode (rectifier operation) for v_g being in its positive half-cycle (v_g>0). During this subinterval, the switches S_1 and S_4 are turned ON, so the capacitors C_1 and C_2 are discharged into the input inductor L_1. As a result, the input current i_{in} is increasing. The output inductor L_o is also being charged by the AC grid, increasing the output current i_o. For v_g being in its negative half-cycle (v_g<0), the same operation is achieved by S_2 being in the ON-state instead of D_2.

Subinterval 2 [$d_1 t_s \leq t < (d_1 + d_2)\ t_s$]: During this subinterval and for v_g being in its positive half-cycle ($vg_>0$), the switch S_P, S_3, and S_4 are turned ON, as shown in Fig. 3(b). The capacitors C_1 and C_2 are being discharged into the output inductor L_o, increasing its current i_o. On the primary side, the input L_1 is being discharged into the battery, decreasing the input current i_{in}. For v_g being in its negative half-cycle (v_g<0), the same operation is achieved by $S_1$and S_2 being in the ON-state instead of S_3 and S_4.

Subinterval 3 [$(d_1 + d_2)\ t_s \leq t < t_s$]: During this subinterval and for v_g being in its positive half-cycle ($vg_>0$), as shown in Fig. 3(c), all switches are turned-OFF. Instead, the diodes D_P, D_1, and D_2 are conducting. As a result, the capacitors C_1 and C_2 are charging through the output inductor L_o, decreasing i_o. The input inductor L_1 is also discharging into the battery, decreasing i_{in}. For v_g being in its negative half-cycle (v_g<0), the same operation is achieved, except D_3 and D_4 are in the ON-state instead of D_1 and D_2.

IV. Second-order Harmonic Elimination

The total power generated by a single-phase AC grid can be written as:

$$S_{\text{in}} = P_{\text{in}} + jQ_{\text{in}} \tag{1}$$

, where:

$$\begin{cases} P_{in} = \dfrac{V_g I_g}{2} \cos\varphi \\ Q_{in} = \dfrac{-V_g I_g}{2} \cos(2\omega t - \varphi) \end{cases} \tag{2}$$

To eliminate the oscillating power Q_{in} containing the second-order harmonic in the battery side, the following equation must be held:

$$Q_{\text{in}} + Q_{\text{Ceq}} = 0 \tag{3}$$

, where $Q_{Ceq} = v^*{}_{Ceq} i_{Ceq}$. As a result, the second-order harmonic component is stored in the capacitor C_{eq} rather than being transferred to the input inductor or the battery side. The desired capacitor voltage $v^*{}_{Ceq}$ is estimated as:

$$v^*_{Ceq}(t) = V_{Cdc} + V_{Cac} \sin(2\omega t + \gamma) \tag{4}$$

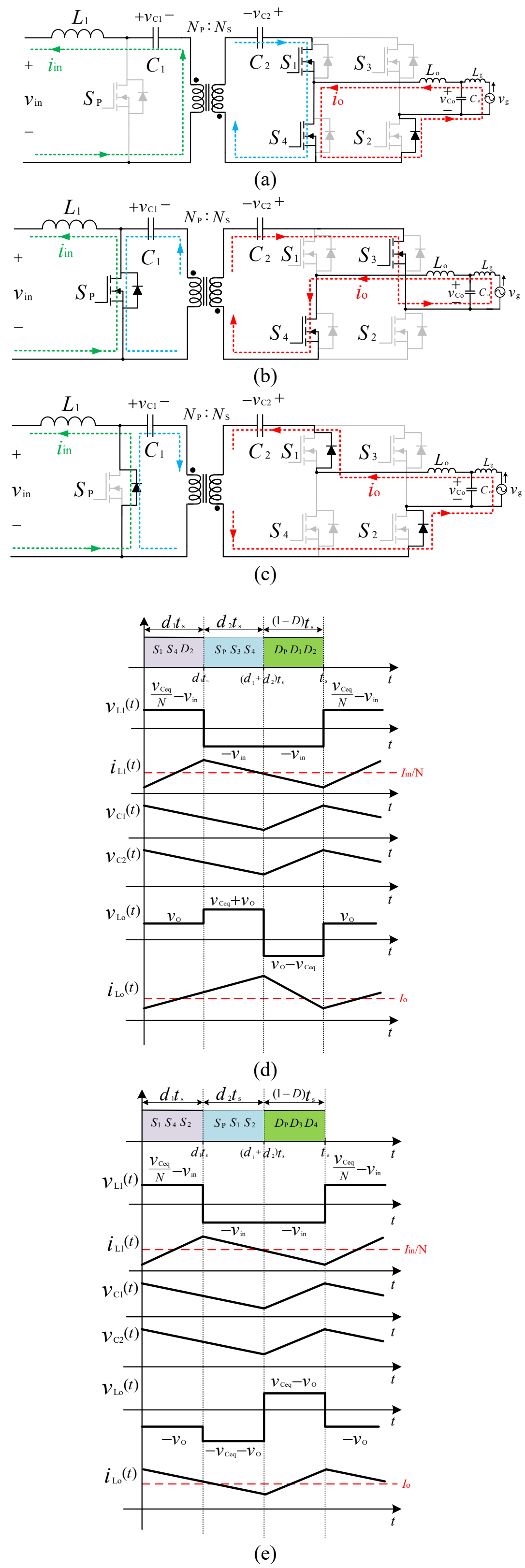

Fig. 3. Rectifier operation (charging mode) of the proposed Cuk-based SM during: (a) $0 < t < d_1 t_s$ (b) $d_1 t_s < t < (d_1 + d_2)\ t_s$ (c) $(d_1 + d_2) t_s < t < t_s$ (d) key waveforms for v_g>0 and (e) for v_g<0

, after substituting (4) in (3), the amplitude and phase of the capacitor voltage $v*_{Ceq}$ can be approximated as:

$$\begin{cases} \gamma = \tan^{-1}\left(\dfrac{\omega L_o I_g \cos(2\varphi) - V_g \sin(2\varphi)}{V_g \cos(2\varphi) + \omega L_g I_g \sin(2\varphi)}\right) \\ V_{Cac} = \dfrac{V_g I_g \cos(2\varphi) + \omega L_o I_g^{\,2} \cos(2\varphi)}{4\omega C_{eq} V_{cdc} \cos\gamma} \end{cases} \tag{5}$$

The average model of the SM can be extracted to calculate the required duty cycle ratios $d_1(t)=t_1/t_s$ and $d_2(t)=t_2/t_s$ of the first and second subintervals in the charging mode. The state vectors $x(t)$ and $u(t)$ are defined as follows:

$$\begin{cases} x(t) = \begin{bmatrix} i_{L1}(t) & v_{Ceq}(t) & i_{Lo}(t) & v_{Co}(t) & i_{Lg}(t) \end{bmatrix}^T \\ u(t) = \begin{bmatrix} v_{in}(t) & v_g(t) \end{bmatrix}^T \end{cases} \tag{6}$$

, where $v_{Ceq}(t)$ and C_{eq} are:

$$\begin{cases} v_{Ceq}(t) = N v_{C1}(t) + v_{C2}(t) \\ C_{eq} = \dfrac{C_1 C_2}{C_1 + N^2 C_2} \end{cases} \tag{7}$$

The average model can be expressed as:

$$\begin{cases} \dot{\bar{x}}(t) = A\,\bar{x}(t) + B\,\bar{u}(t) \\ y(t) = C\,\bar{x}(t) \end{cases} \tag{8}$$

$$\begin{cases} \dot{\bar{i}}_{L_1}(t) = \dfrac{d_1}{NL_1} v_{C_{eq}}(t) - \dfrac{1}{L_1} v_{in}(t) \\ \dot{\bar{v}}_{C_{eq}}(t) = \dfrac{-d_1}{NC_{eq}} i_{L_1}(t) + \dfrac{1 - d_1 - 2d_2}{C_{eq}} i_{L_o}(t) \\ \dot{\bar{i}}_{L_o}(t) = \dfrac{-(1 - d_1 - 2d_2)}{L_o} v_{C_{eq}}(t) + \dfrac{1}{L_o} v_{C_o}(t) \\ \dot{\bar{v}}_{C_o}(t) = \dfrac{-1}{C_o} i_{L_o}(t) + \dfrac{1}{C_o} i_{L_g}(t) \\ \dot{\bar{i}}_{L_g}(t) = \dfrac{-1}{L_g} v_{C_o}(t) + \dfrac{1}{L_g} v_g(t) \end{cases} \tag{9}$$

The duty cycle ratios $d_1(t)$ and $d_2(t)$ can be calculated to store the second-order harmonic within the capacitor C_{eq}. Since the battery current (input current $i_{L1}(t)$) must remain constant, the first row in (9) should be held as:

$$\dot{\bar{x}}_1(t) = \dot{\bar{i}}_{L1}(t) = \frac{d_1(t)}{NL_1} v^*_{Ceq}(t) - \frac{1}{L_1} v_{in}(t) = 0 \tag{10}$$

Therefore, the duty ratio of the first subinterval $d_1(t)$ is calculated as:

$$d_1(t) = \frac{v_{in}(t)}{v^*_{Ceq}(t)} \tag{11}$$

and using the third row in (5), the duty ratio of the second subinterval $d_2(t)$ is obtained as:

$$d_2(t) = \frac{L_2 \dot{\bar{i}}_{L_o}(t) - v_{Co}(t) - v_{in}(t) + v^*_{Ceq}(t)}{2v^*_{Ceq}(t)} \tag{12}$$

, where $v_{Co}(t)=v_g(t)=V_g\sin(\omega t)$ and $i_{Lo}(t)=i_{Lg}(t)=I_g\sin(\omega t+\varphi)$ are the grid voltage and current, respectively. V_g and I_g are the amplitude of the grid voltage and current, and $\omega=2\pi f$ is the grid frequency (f=50Hz). The phase shift between the grid voltage and current is represented by φ.

Fig. 4 illustrates the block diagram of the AC/DC mode controller when the power flows from the AC grid to the batteries. As shown, classical PR and PI controllers are employed to regulate input and output voltages.

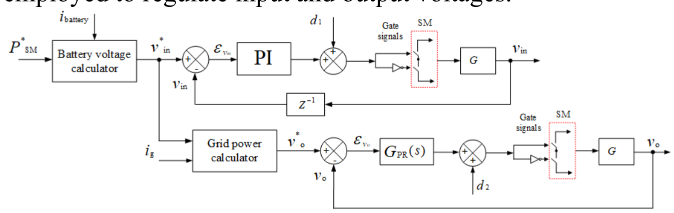

Fig. 4. Block diagram of the controller in the charging mode (AC/DC mode)

The closed-loop system's root loci are plotted using the SISOTOOL interactive toolbox in MATLAB/SIMULINK to provide a practical approach for determining appropriate PR controllers' gains (k_p and k_r). The system parameters listed in Table. 1 are used for the simulations. Fig. 5 illustrates the resulting root loci. In Fig. 5(a), the resonant gain k_r is varied within the range of [1:10], while the proportional gain k_p is held constant at 1. In Fig. 5(b), k_p is adjusted within the range [0.1:2], while k_r remains fixed at 1. To ensure system stability, minimize overshoot, and expand the controller's bandwidth (BW), the gain values are chosen within these specified ranges. By setting k_p to 1.2 and k_r to 6, stable system performance is achieved that neither compromises BW nor stability.

TABLE 1. SYSTEM PARAMETERS

Parameters	**Value**
Number of SMs	9
SM inductors	L_1 = 0.5 mH, L_2 = 10 mH
SM capacitors	C_1 = C_2 = 10 μF - C_o = 1 μF
SM rated power	P_{SM}=*4.2* kW
Switching frequency	f_s = 50 kHz
Turn ratio	N_P: N_S = 1
PV module	P_m = 420W, V_{mp} = 48.73V, I_{mp} = 8.62
Battery voltage	V_{bat} = 200V
Grid voltage	$V_{g(rms)}$ = 24.5 kV
Grid frequency	f = 50 Hz

V. POWER LOSSES AT THE SM LEVEL

The currents passing through the primary-side switch S_P and secondary-side switches and diodes are shown in Fig. 6. The conduction losses related to S_P can be approximated as:

$$P_{\mathrm{Loss(Primary)}} = P_{SP} = R_{\mathrm{ON}} I^2_{SP(\mathrm{RMS})} \tag{13}$$

The diode D_P is conducted over a short period of the cycle and its power losses are ignored.

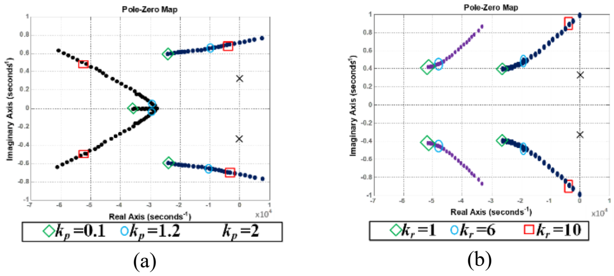

Fig. 5. The closed-loop system's root loci (pole-zero map)

For the sinusoidal output voltage $v_{Co}(t)=v_g(t)=V_g\sin(\omega t)$ and current $i_{Lo}(t)=i_{Lg}(t)=I_g\sin(\omega t+\varphi)$, the envelope of the switch current $i_{env1}(t)$ shown in Fig. 6(a) can be expressed as:

$$i_{S_P}(t)=i_{L1}(t)=i_{env1}(t)=\frac{d(t)}{1-d(t)}Ni_{L_o}(t) \tag{14}$$

, with $d(t)$ being:

$$d(t)=\frac{v_{C_o}(t)}{Nv_{in}(t)+v_{C_o}(t)} \tag{15}$$

, therefore, $i_{env1}(t)$ can be re-written as:

$$i_{env1}=\frac{V_g\sin(\omega t)I_g\sin(\omega t+\varphi)}{V_{in}}=\frac{V_gI_g}{2V_{in}}\left(\cos(\varphi)-\cos(2\omega t+\varphi)\right) \tag{16}$$

The Root-Mean-Square (RMS) value of the switch current $I_{S_P(RMS)}$ is calculated as:

$$I^2_{S_P(RMS)}=\frac{1}{T}\int_0^T(i_{env1}(t))^2d(t)dt=$$
$$\frac{1}{2}\left(\frac{V_gI_g}{2V_{in}}\right)^2\left(2\cos^2(\varphi)V_g+V_g-\frac{\cos(2\varphi)}{2V_g^2}(V_g^2-4V_{in}^2)\right.$$
$$\left.+\frac{\cos(2\varphi)}{2V_g^4}(V_g^4-12V_{in}^2V_g^2+16V_{in}^4)+\frac{8V_{in}^2\cos^2(\varphi)}{V_g^2}\right) \tag{17}$$

If the SM operates at the unity power factor (i.e., $\varphi=0$), $I_{S_P(RMS)}$ can be re-written as:

$$I^2_{S_P(RMS)}=\frac{1}{2}\left(\frac{V_gI_g}{2V_{in}}\right)^2\left(3V_g-\frac{1}{2V_g^2}(V_g^2-4V_{in}^2)+\right.$$
$$\left.\frac{1}{2V_g^4}(V_g^4-12V_{in}^2V_g^2+16V_{in}^4)+\frac{8V_{in}^2}{V_g^2}\right) \tag{18}$$

The power losses related to the semiconductor devices at the secondary side are approximated as:

$$P_{Loss(Secondary)}=2(R_{ON}I^2_{S3\text{-}4(RMS)}+\bar{I}_{D_{3\text{-}4}}V_{DF}) \tag{19}$$

The current $i_{env2}(t)$ shown in Fig. 6(b) can be expressed as:

$$i_{env2}(t)=i_{S_{3\text{-}4}}(t)=i_{Lo}(t) \tag{20}$$

The RMS value of this current $I_{S_{3\text{-}4}(RMS)}$ is calculated as:

$$I^2_{S3\text{-}4(RMS)}=\frac{1}{T}\int_0^T(i_{env2}(t))^2d(t)dt=$$
$$\frac{2V_gI_g^2+\cos(2\varphi)I_g^2}{4}-\frac{I_g^2\cos(2\varphi)(V_g^2-4NV_{in}^2)}{4V_g^2} \tag{21}$$

If the inverter operates at the unity power factor (i.e., $\varphi=0$), $I_{S_{3\text{-}4}(RMS)}$ can be re-written as:

$$I^2_{S3\text{-}4(RMS)}=\frac{2V_gI_g^2+I_g^2}{4}-\frac{I_g^2(V_g^2-4NV_{in}^2)}{4V_g^2} \tag{22}$$

The average value of the diode current $\bar{I}_{D_{3\text{-}4}}$ is computed as:

$$\bar{I}_{D_{3\text{-}4}}=\frac{1}{T}\int_0^T(1-d(t))i_{L_o}(t)dt=\frac{NV_{in}I_g\cos(\varphi)}{V_g} \tag{23}$$

If the inverter operates at the unity power factor (i.e., $\varphi=0$), $\bar{I}_{D_{3\text{-}4}}$ can be re-written as:

$$\bar{I}_{D_{3\text{-}4}}=\frac{NV_{in}I_g}{V_g} \tag{24}$$

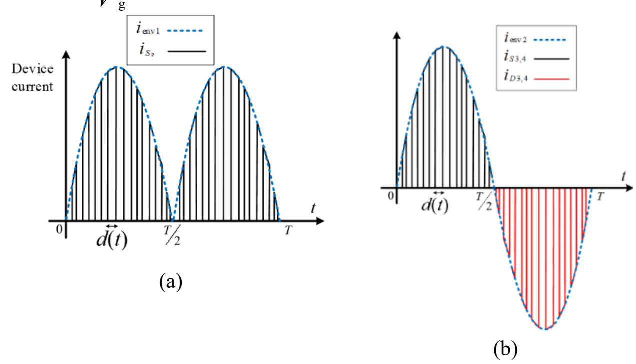

Fig. 6. Current flowing through (a) S_P (b) $S_{3\text{-}4}$ and $D_{3\text{-}4}$

VI. Experimental Verification

Fig. 7 shows the scaled-down prototype of the modular PV-powered grid-tied EV charger together with measurement and control circuits.

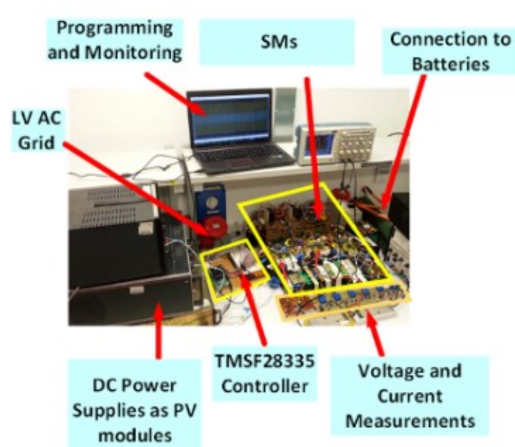

Fig. 7. Scaled-down prototype

To validate the performance of the proposed modular topology, experimental results are presented for the DC/AC mode. To test stability, the output power of the SMs was suddenly decreased by more than 75%, dropping from around 3 kW to approximately 750 W. This drop in the power could mimic partial shading or a fault in one of the battery segments. Initially, the output power had been raised to 3 kW within 100 ms. The grid current ig is shown in Fig. 8(b). After the abrupt reduction in Pout, the grid current drops to 25% from its maximum value after 250 ms. Despite the drastic change in output power, the output voltages of the first four SMs shown in Fig. 8(c) remain constant. Despite an undershoot in the output power, the input currents of the first SM in each of the three phases shown in Fig. 8(d) exhibit stability and do not show significant fluctuations. These results show that the proposed system exhibits robustness even in the event of abrupt changes in the output power of the modular topology.

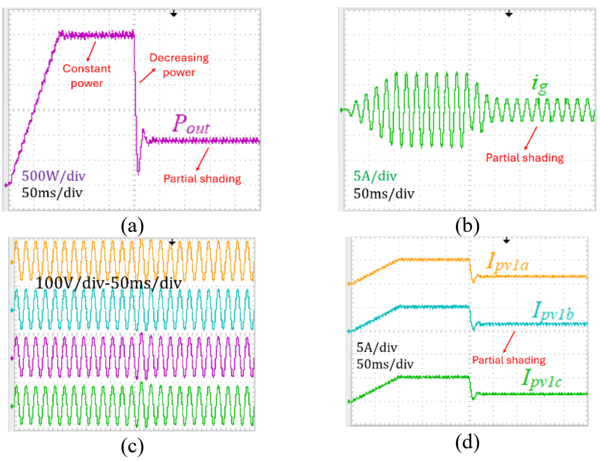

Fig. 8. Experimental results in the DC/AC mode for a sudden 75% drop in power (a) The output power of the SMs (b) Grid current (c) Output voltage of the 4 SMs in phase "*a*" (d) The input currents of the 4 SMs in phase "*a*"

VII. Conclusion

A modular topology is presented in this paper to interface with the PV modules, EV batteries, and the AC grid. The proposed topology can operate in all the operating modes of DC/DC, DC/AC, and AC/DC modes. The experimental results using a scaled-down prototype confirm that the batteries respond to variations in the PV power. In addition, to verify the stability of the proposed modular topology, the output power of the SMs was abruptly reduced by over 75%, to mimic a partial shading or a fault in one of the battery segments. Despite an undershoot in the output power, the input currents of the SM exhibit stability and do not show significant fluctuations. These results show that the proposed system exhibits robustness even in the event of abrupt changes in the output power.

References

[1]. M. Niroomand, F. Nasr Esfahani, S. M. Tripathi, and S. Padmanaban, "Converter technologies for PV systems: A comprehensive review," *Energy Conversion Systems: An Overview*, pp. 1-58, 2021.

[2]. M. Niroomand, F. Nasr Esfahani, S. M. Tripathi, and S. Padmanaban, "Control Structures of Grid-Tied Photovoltaic Systems," pp. 59-133, 2021.

[3]. F. Nasr Esfahani, A. Darwish, and A. Massoud, "PV/battery grid integration using a modular multilevel isolated SEPIC-based converter," Energies, vol. 15, no. 15, pp. 5462, 2022.

[4]. F. Nasr Esfahani, A. Darwish, B. W. Williams. "Power converter topologies for grid-tied solar photovoltaic (PV) powered electric vehicles (EVs)—A comprehensive review," in *Energies*, vol. 15, no. 13, 2022, pp. 4648.

[5]. F. Nasr Esfahani, A. Darwish, and X. Ma, "Design and Control of a Modular Integrated On-Board Battery Charger for EV Applications with Cell Balancing," *Batteries*, vol. 10, no. 1, pp. 17, 2024.

[6]. F. Nasr Esfahani, and A. Darwish, "Regenerative Braking for EVs Using PMSM with CHB as Bidirectional Traction Converter," In *2022 IEEE 16th International Conference on Compatibility, Power Electronics, and Power Engineering (CPE-POWERENG)*, pp. 1-7. IEEE, 2022.

[7]. F. Nasr Esfahani, A. Darwish, X. Ma, and P. Twigg, "Non-Integrated and Integrated On-Board Battery Chargers (iOBCs) for Electric Vehicles (EVs): A Critical Review," *Energies*, vol. 17, no. 10, pp. 2285, 2024.

[8]. A. D. Badawy et al., "Low-Voltage Control Circuits of Formula Student Electric Racing Cars," *Hardware*, vol. 2, no. 3, pp. 190-222, 2024.

[9]. G. Rajendran, C. A. Vaithilingam, N. Misron, K. Naidu, and M. R. Ahmed, "Voltage Oriented Controller Based Vienna Rectifier for Electric Vehicle Charging Stations," in *IEEE Access*, vol. 9, 2021, pp. 50798-50809.

[10]. Q. Chen, J. Xu, F. Zeng, R. Huang, and L. Wang, "An Improved Three-Phase Buck Rectifier with Low Voltage Stress on Switching Devices," in *IEEE Trans. Power Electron.*, vol. 36, no. 6, 2020, pp. 6168-6174.

[11]. Q. Chen, J. Xu, L. Wang, R. Huang, and H. Ma, "Analysis and improvement of the effect of distributed parasitic capacitance on high-frequency high-density three-phase buck rectifier," in *IEEE Trans. Power Electron.*, vol. 36, no. 6, 2020, pp. 6415-6428.

[12]. A. Ul-Haq, C. Cecati, and E. A. Al-Ammar, "Modeling of a photovoltaic-powered electric vehicle charging station with vehicle-to-grid implementation," in *Energies*, vol. 10, no. 4, 2016, p. 4.

[13]. A. R. Bhatti, Z. Salam, M. J. B. Abdul, and K. P. Yee, "A comprehensive overview of electric vehicle charging using renewable energy," *in Int. J. Power Electron. Drive Syst.*, vol. 7, no. 1, 2016, pp. 114-123.

[14]. Y. Xuan, X. Yang, W. Chen, T. Liu, and X. Hao, "A novel three-level CLLC resonant DC–DC converter for bidirectional EV charger in DC microgrids," in *IEEE Trans. Ind. Electron.*, vol. 68, no. 3, 2020, pp. 2334-2344.

[15]. Y. Yan, H. Bai, A. Foote, and W. Wang, "Securing full-power-range zero-voltage switching in both steady-state and transient operations for a dual-active-bridge-based bidirectional electric vehicle charger," in *IEEE Trans. Power Electron.*, vol. 35, no. 8, 2019, pp. 7506-7519.

[16]. S. A. Assadi, H. Matsumoto, M. Moshirvaziri, M. Nasr, M. S. Zaman, and O. Trescases, "Active saturation mitigation in high-density dual-active-bridge DC–DC converter for on-board EV charger applications," in *IEEE Trans. Power Electron.*, vol. 35, no. 5, 2019, pp. 4376-4387.

[17]. G. R. C. Mouli, J. Schijffelen, M. van den Heuvel, M. Kardolus, and P. Bauer. "A 10-kW solar-powered bidirectional EV charger compatible with chademo and COMBO," in *IEEE transactions on Power electronics*, vol. 34, no. 2, 2018, pp. 1082-1098.

[18]. S. A. Khan, M. R. Islam, Y. Guo, and J. Zhu. "A new isolated multi-port converter with multi-directional power flow capabilities for smart electric vehicle charging stations," in *IEEE Transactions on Applied Superconductivity*, vol. 29, no. 2, 2019, pp. 1-4.

[19]. A. K. Bhattacharjee and I. Batarseh. "An interleaved boost and dual active bridge-based single-stage three-port DC/DC/AC converter with sine PWM modulation," in *IEEE Transactions on Industrial Electronics*, vol. 68, no. 6, 2020, pp. 4790-4800.

[20]. V. Monteiro, J. G. Pinto, and J. L. Afonso. "Experimental validation of a three-port integrated topology to interface electric vehicles and renewables with the electrical grid," in *IEEE Transactions on Industrial Informatics*, vol. 14, no. 6, 2018, pp. 2364-2374.